

A circular equilibrium model for local gyrokinetic simulations of ion temperature gradient fluctuations in reversed field pinches

Varun Tangri,¹ P. W. Terry,¹ and R. E. Waltz²

¹*Department of Physics, University of Wisconsin-Madison, 1150 University Avenue, Madison, Wisconsin 53706R, USA*

²*General Atomics, San Diego, California 92186, USA*

(Received 18 December 2010; accepted 28 March 2011; published online 31 May 2011)

A simple large-aspect-ratio (R_0/r) circular equilibrium model is developed for low-beta reversed field pinch (RFP) geometry. The model is suitable for treating small scale instability and turbulent transport driven by ion temperature gradient (ITG) and related electron drift modes in gyrokinetic simulations. The equilibrium model is an RFP generalization of the common tokamak s - α model to small safety factor (q), where the poloidal field dominates the toroidal field. The model accommodates the RFP toroidal field reversal (where q vanishes) by generalizing the cylindrical force-free Bessel function model (BFM) [J. B. Taylor, Phys. Rev. Lett. **33**, 1139 (1974)] to toroidal geometry. The global equilibrium can be described in terms of the RFP field reversal and pinch parameters [F, Θ]. This new toroidal Bessel function model (TBFM) has been incorporated into the gyrokinetic code GYRO [J. Candy and R. E. Waltz, J. Comput. Phys. **186**, 545 (2003)] and used here to explore local electrostatic ITG adiabatic electron instability rates for typical low- q RFP parameters. © 2011 American Institute of Physics. [doi:10.1063/1.3581072]

I. INTRODUCTION

Ion temperature gradient (ITG) driven short-scale micro-instabilities (i.e., those satisfying $k_\theta \rho_i < 1$, where k_θ is the poloidal wavenumber and ρ_i is the ion gyroradius) are ubiquitous in magnetically confined plasmas. The ITG instability has been of great interest in theoretical and experimental tokamak studies¹ for many years. These studies suggest that ITG and related nonadiabatic electron modes (trapped electron modes at $k_\theta \rho_i < 1$ and electron temperature gradient modes at $k_\theta \rho_i > 1$ where the ions are adiabatic) account for essentially all the high-toroidal-wavenumber turbulent transport in the energy, particle, and momentum channels of the tokamak.¹

The reversed field pinch (RFP) parameter space is an ultra-low- q ($B_\theta \sim B_\phi$, $q \ll 1$), negative shear ($dq/dr < 0$) regime with average bad curvature. It has rarely been investigated from the viewpoint of ITG. This is because current-driven tearing modes are believed to dominate core transport in such machines. The control and mitigation of tearing mode instabilities in RFPs has therefore been the first priority.

However, in the last few decades, global tearing modes in an RFP have been significantly reduced by using a current profile that is externally controlled.² It is thought that under these circumstances, small scale modes should become a significant factor in RFP particle and heat transport just as in a tokamak. However, what type of mode will dominate transport has never been determined. A complete understanding of linear stability and the saturation of short-scale microinstabilities will require both detailed experimental diagnostics and, for accurate results, massively parallel, nonlinear, full radius, gyrokinetic simulations. The ITG instability in the RFP has received attention only relatively recently. Analytical work has been subject to approximations,³ including fluid reductions.⁴ More recently linear gyrokinetic flux-tube simulations have been performed.^{5,6} Determination of the role of

electrostatic ITG-driven particle and heat transport in enhanced confinement RFP plasmas could lead to improvement in our understanding and further refinement of the enhanced confinement procedure.

The primary goal of this manuscript is to lay essential groundwork for numerical investigation of ion temperature gradient driven turbulence in an RFP geometry. This includes a simple large-aspect-ratio circular equilibrium model using a small set of parameters and a detailed comparison with other equilibria. Numerical and analytical studies of ITG require detailed information about the equilibrium. This includes the equilibrium density, temperature, and current profiles, which, along with boundary conditions, can be used to compute the toroidal and poloidal magnetic fields and their curvature in space. The role of this information in determining the stability of turbulence is well documented.⁷ The most common zero-beta RFP equilibria, the Bessel function model (BFM),⁸ or the modified Bessel function model (MBFM),⁹ have been obtained in cylindrical geometry as a solution of the force-free state:

$$\nabla \times B = \mu B, \quad (1)$$

where B is the magnetic field and μ , frequently, is a constant. In other words, the BFM is specified by the eigenvectors of the curl operator in cylindrical geometry.

On the other hand, existing gyrokinetic simulation codes have been designed around the large-aspect-ratio (R_0/r) shifted-circle tokamak s - α model where the toroidal field completely dominates the poloidal field with $q(r) > 1$. In this paper, we generalize the tokamak s - α model equilibrium to large r/R_0q while treating the toroidal field reversal (where q vanishes and turns negative beyond) by generalizing the cylindrical force-free BFM equilibrium to toroidal geometry (adding toroidal field curvature to the fields).

Simple shifted-circle, large-aspect-ratio, tokamak equilibria have been obtained in the past by expanding the Grad-Shafranov equation:¹⁰

$$\Delta^* \Psi = -\mu_0 R^2 p' - F \frac{dF}{d\Psi}, \quad (2)$$

where the toroidal magnetic field is given by $B_\phi \equiv F(\Psi)/R$, Ψ is the flux function, and all other symbols here are explained in detail in Sec. II. The Grad-Shafranov equation has been solved analytically using simple approximations for $F(\Psi)$ and $p' \equiv dp/d\Psi$ to give analytical tractability. In the limit of zero-beta ($p \rightarrow 0$) and infinite aspect ratio (cylinder) with $F(\Psi) = f_0 = \text{const.}$, the toroidal magnetic field is given by $B_\phi \equiv F(\Psi)/R \sim f_0/R$, with $B_\theta \ll B_\phi$ and $q \gg 1$ in the simplest limit. A large number of studies have concentrated on this limit.

The BFM is cylindrical, but could trivially be adapted to toroidal geometry by stipulating that $B_\phi = F(\Psi)/R$ and leaving B_θ unchanged. We will show that this prescription is inconsistent with the Grad-Shafranov equation for its treatment of B_θ . Hence, we must develop consistent approximations to the Grad-Shafranov equation. Noting a variety of simplifying approximations,^{11–14} we assume very low beta and make the simple assumption $FF' \propto (\Psi - \Psi_s)$. This is inspired from actual MST equilibria, *e.g.*, Fig. 7(c) of Anderson *et al.*¹⁵ Using this new toroidal Bessel function model (TBFM), we address the problem of microturbulence in an RFP, by modifying GYRO,¹⁶ a state-of-the-art computational code with many useful features. GYRO is a flexible microturbulence code, which provides us the capability to perform either flux-tube (with flat profiles) or global simulations in a general geometry.^{17–20} As a special case, it also allows us to simulate turbulence in a shifted-circle, low-beta geometry, in addition to the use of realistic experimental data in the eqdisk format. It must be noted that GYRO assumes an equilibria that is a solution of the Grad-Shafranov equation or $B_\phi \equiv F(\Psi)/R$.

We illustrate the new TBFM RFP equilibrium modifications made to GYRO by computing the linear growth rate of the ITG instability and comparing it with growth rate calculations using the common s - α and Miller equilibrium representations. Miller geometry is a generalization of the local large-aspect-ratio shifted circular s - α model to an equilibrium representation that is appropriate for finite-aspect ratio and high beta and that accommodates shifted flux surfaces with an elliptical cross section, elongation, and triangularity. The Miller representation can be fitted to experimental global equilibrium profiles. Toroidal field reversal is easily accommodated when the poloidal flux or the midplane minor radius is used as a flux surface label. We show that the three equilibria yield different growth rates. The TBFM equilibria growth rates differ substantially from the “ s - α ” model for RFP parameters but are close to those predicted using the Miller equilibrium.

This manuscript is organized as follows. In Sec. II, the equilibrium is introduced. Two special cases are developed in B, including a simple circular limit of the equilibrium. The computed equilibria are shown to correspond well with equilibrium reconstruction from MSTFIT.²¹ In Sec. III, we

describe the implementation in GYRO of the equilibria developed in Sec. II. The linear stability of ITG modes using GYRO in a typical RFP flux-tube is presented in Sec. IV. Conclusions are discussed in Sec. V. A detailed mathematical description of the derivation of the equilibrium, which includes the shift, is presented in the Appendix.

II. MODEL EQUILIBRIA

In Sec. II A, we solve the Grad-Shafranov (GS) equation for an approximate large-aspect-ratio, shifted-circular RFP equilibrium by generalizing the common force-free ($\nabla \times \vec{B} = \mu \vec{B}$) cylindrical Bessel function model (BFM) (Ref. 8) to account for toroidal curvature in the toroidal field as well as the Shafranov shift. The toroidal and poloidal field of the BFM can be written as $B_\phi^{\text{BFM}}(r) = B_0 J_0(\mu r)$ and $B_\theta^{\text{BFM}}(r) = B_0 J_1(\mu r)$, where J_0 and J_1 are the first and second Bessel functions and $\mu = 2\Theta/a$. The quantity Θ is the common RFP wall pinch parameter $\Theta = \langle B_\theta \rangle^{\text{wall}} / \langle B_\phi \rangle^{\text{vol}} = \mu a/2$. A second important RFP parameter relating to the equilibrium is the wall toroidal field reversal parameter is $\mathbf{F} = \langle B_\phi \rangle^{\text{wall}} / \langle B_\phi \rangle^{\text{vol}} = \Theta J_0(2\Theta) / J_1(2\Theta)$ (Ref. 10). The generalized and approximate GS solution we are deriving is best for lower Θ because it becomes less accurate at high Θ .

In Sec. II B, we drop the radial (Shafranov) shift of the magnetic center (needed when the gradient in the poloidal beta is high) and rewrite the large-aspect-ratio circular RFP equilibrium as the TBFM with poloidal field $B_\theta^{\text{TBFM}}(r) = (R_0/R) B_\theta^{\text{BFM}}(r)$ and toroidal field $B_\phi^{\text{TBFM}}(r) = (R_0/R) B_\phi^{\text{BFM}}(r)$. The toroidal field is now in the form $F(\Psi)/R$ required for standard tokamak gyrokinetic codes like GYRO.¹⁶ In the circular limit, the major radius is $R = R_0[1 + (r/R_0) \cos \theta]$ with θ the usual poloidal angle from the outboard-midplane and r the (midplane) minor radius. The TBFM generalizes the large-aspect-ratio shifted circular tokamak s - α model to include the neglected poloidal field. (However, we have dropped the radial shift.) The ratio of poloidal to toroidal magnetic fields is $J_1/J_0 = r/R_0 q$, where $q(r)$ is the safety factor.

A. Low- large-aspect-ratio shifted circular RFP equilibrium

We assume that the MST flux surface is approximately circular and is centered at its magnetic center C_m (see Fig. 1). It should be noted that some of the notation used in Fig. 1 differs from that of Ref. 16. Here, we use several radial coordinates. The variable \hat{r} is the cylindrical radial coordinate (normalized to the last closed flux surface radius a) and is not a flux function except on the boundary. The variable r , which is the radius of a surface, is a flux function and $\bar{r} \equiv r/a$. As will be explained later, the variable ϱ is the areal coordinate used as a measure of enclosed toroidal flux as in Ref. 16 and does not have one-to-one correspondence to r for an RFP, as we discuss in Sec. II C. The point $\hat{r} = 0$ is the geometric center, whereas $r = 0$ is the magnetic center. The boundary is assumed circular (indicated by a solid line at $r = a$) and centered at $r = 0$. Note that the surfaces have been assumed circular but shifted. We also define $\varepsilon_a = a/R_0$ (inverse aspect

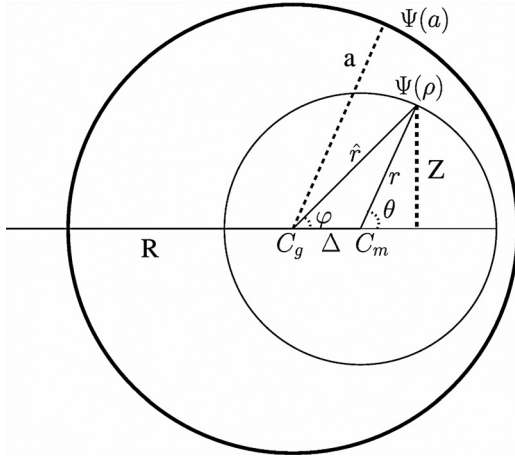


FIG. 1. A toroidal device with geometric center C_g and minor radius a is illustrated. Here, R and Z are the usual cylindrical coordinates.

ratio), where R_0 is the major radius at the flux surface center and $r = a$ is the minor radius at the last closed flux surface.

An axisymmetric toroidal MHD equilibrium is assumed such that each flux surface is characterized by a unique value Ψ . In the usual cylindrical coordinates (R, ϕ', z) , this surface may be characterized by the variables $R_s(\Psi)$ and $Z_s(\Psi)$, where the subscript s stands for surface. The solution is usually determined from the Grad-Shafranov equation¹⁰ in the large-aspect-ratio limit (i.e., $\varepsilon_a \equiv a/R_0 \ll 1$) via a series expansion. This equation is as follows:

$$\begin{aligned} \Delta^* \Psi &\equiv R^2 \nabla \cdot \left(\frac{\nabla \Psi}{R^2} \right) = R \frac{\partial}{\partial R} \left(\frac{1}{R} \frac{\partial \Psi}{\partial R} \right) + \frac{\partial^2 \Psi}{\partial Z^2} \\ &= -\mu_0 R^2 p' - F \frac{dF}{d\Psi}, \end{aligned} \quad (3)$$

where

$$B = (1/R) \nabla \Psi \times \mathbf{e}_\phi + (F/R) \mathbf{e}_\phi, \quad (4)$$

so that $RB_\phi = F(\Psi)$ and $B_\theta = |\vec{\nabla} \Psi|/R$.

Simple approximations for $F(\Psi)$ and $p' \equiv dp/d\Psi$ that have been developed for analytical tractability, e.g., the Solov'ev equilibrium¹¹ [$F^2(\Psi) = 2B\Psi + F_0^2$, $p(\Psi) = (A/\mu_0)\Psi$], the Herrnegger-Maschke solutions^{12,13} [$F^2(\Psi) = D\Psi^2 + F_0^2$], etc. Perhaps the most useful of these is the large-aspect-ratio, finite-beta equilibria, frequently used in tokamak microinstability studies,¹⁴

$$F(\Psi) = f_0 \left(1 - \frac{R_0^2 \mu_0 p}{f_0^2} + \frac{1}{2} \left(\frac{R_0^2 \mu_0 p}{f_0^2} \right)^2 + \frac{f_2}{f_0} + \dots \right), \quad (5)$$

where p is the pressure and the terms proportional to $R_0^2 \mu_0 p / f_0^2$ are finite-beta, finite-aspect ratio corrections. Even here, simple forms for $p(\Psi)$ and f_0/f_2 were chosen in Ref. 14 so that Eq. (2) is linear and easy to solve.

For mathematical convenience, we now make a transformation from the usual (R, ϕ', Z) coordinates to a coordinate system (\hat{r}, θ, ϕ) with origin at the geometric center C_g (see Fig. 1): $R = R_0 + a\hat{r} \cos \varphi$, $Z = a\hat{r} \sin \varphi$, and $\phi' = -\phi$. In these coordinates, we have

$$\begin{aligned} &\left[\frac{\partial^2}{\partial \hat{r}^2} + \frac{1}{\hat{r}} \frac{\partial}{\partial \hat{r}} + \frac{1}{\hat{r}^2} \frac{\partial^2}{\partial \varphi^2} - \frac{a}{R_0 + a\hat{r} \cos \varphi} \left(\cos \varphi \frac{\partial}{\partial \hat{r}} - \frac{\sin \varphi}{\hat{r}} \frac{\partial}{\partial \varphi} \right) \right] \Psi \\ &= -4\pi R^2 a^2 \frac{dp}{d\Psi} - a^2 F \frac{dF}{d\Psi}, \end{aligned} \quad (6)$$

where

$$\begin{aligned} B_\phi &= F(\Psi)/R, \quad B_\theta = B \cdot \mathbf{e}_\theta = -\frac{1}{aR} \frac{\partial \Psi}{\partial \hat{r}}, \quad \text{and} \\ B_r &= B \cdot \mathbf{e}_r = \left(\frac{1}{a\hat{r}R} \right) \frac{\partial \Psi}{\partial \theta}. \end{aligned} \quad (7)$$

To simplify the analysis, we have normalized the length to minor radius a (thus $\hat{r} = 1$ on the boundary). When the shift Δ collapses to zero (or is ignored), $\hat{r} \rightarrow r$ and $\varphi \rightarrow \theta$ (see Fig. 1). At this point, we can simplify Eq. (6) using the approximation mentioned in the Introduction,

$$\frac{dF(\Psi)}{d\Psi} = \mu + \hat{f}(\Psi) O(\varepsilon_a^2). \quad (8)$$

Through $O(\varepsilon)$, this expression yields

$$F(\Psi) = \mu(\Psi - \Psi_s), \quad (9)$$

where Ψ_s is a constant of $O(\varepsilon_a)$ or smaller. This approximation provides a connection to simplified RFP equilibria as follows. The force-free equation $\nabla \times B = \mu B$ can be decomposed into two equations $j_\phi = \mu B_\phi / \mu_0$ and $j_\theta = \mu B_\theta / \mu_0$. The second equation satisfies the Grad-Shafranov equation because of the short poloidal circuit. The form consistent with the Grad-Shafranov equation is $j_\theta = (dF/d\Psi)(B_\theta / \mu_0)$, which implies $dF/d\Psi = \mu$. When this expression is assumed to hold to $O(\varepsilon)$, consistent with Eq. (9), and finite-beta is ignored, the solution of the Grad-Shafranov equation is a function of two parameters. These are $\mu = 2\Theta/a$ and r/a , where Θ is the RFP pinch parameter and a is the minor radius. The derivation is given in the Appendix. This simplified Grad-Shafranov solution reproduces low- Θ MST equilibria while being useful for toroidal ITG studies. It also reduces to the cylindrical BFM model.

The solution of the Grad-Shafranov equation for a circular shifted RFP equilibrium is obtained by substituting Eqs. (8) and (9) into Eq. (6). The average poloidal beta is assumed to be order ε_a^2 , i.e., $\beta_p \sim O(\varepsilon_a^2)$, which allows the neglect of the $dp/d\Psi$ term in Eq. (6). The resulting form of Eq. (6) is expanded in powers of ε and solved order by order up to $O(\varepsilon)$. Constants of integration are chosen to satisfy the wall boundary conditions. From the solution

$$\Psi(r/a) = \frac{aB_0}{2\Theta} [J_0(2r\Theta/a) - J_0(2\Theta)], \quad (10)$$

$$\varepsilon_a \Delta(r/a) = \frac{a}{4} \left[\sqrt{\pi} \frac{\mathcal{F}(2r\Theta/a)}{J_1(2\Theta)} (r/a)^2 + \frac{2\delta}{\Theta} \right], \quad (11)$$

where $\delta = -\sqrt{\pi}(\Theta/2)\mathcal{F}(2\Theta)/J_1(2\Theta)$ and \mathcal{F} is a combination of Bessel functions. [See the Appendix, Eq. (A10).] From this solution,

$$B_\phi = B_0 J_0(2r\Theta/a) [1 - \varepsilon_a(r/a) \cos \theta], \quad (12)$$

$$B_\theta = -\frac{1}{R} \frac{\partial \Psi}{\partial r} (1 - \varepsilon_a \cos \theta \Delta') \\ = B_0 J_1(2\Theta r/a) [1 - \varepsilon_a (r/a + \Delta') \cos \theta], \quad (13)$$

where $\Delta' = \partial_r \Delta(r/a)$. Finally, in this coordinate system, $B_r(a) = 0$ identically since Ψ has no dependence on θ .

B. Low- Θ RFP toroidal Bessel function model

Dropping the radial Shafranov shift Δ' of the magnetic center in Eq. (13) (which is only needed when the gradient in the poloidal beta is high), we can define from Eqs. (12) and (13) the large-aspect-ratio circular RFP approximate equilibrium or TBFM:

$$B_t = \frac{B_0 J_0[2\Theta r/a]}{[1 + (r/R_0) \cos \theta]}, \quad (14)$$

$$B_p = \frac{B_0 J_1[2\Theta r/a]}{[1 + (r/R_0) \cos \theta]}, \quad (15)$$

where the major radius is $R = [1 + (r/R_0) \cos \theta]$ with θ the usual poloidal angle from the outboard-midplane and r the (midplane) minor radius.

The toroidal field is now in the form $F(\Psi)/R$ required for standard tokamak gyrokinetic codes like GYRO.¹⁶ It is convenient to define $B_\phi^{\text{TBFM}}(r) = (R_0/R) B_\phi^{\text{BFM}}(r)$ and $B_\theta^{\text{TBFM}}(r) = (R_0/R) B_\theta^{\text{BFM}}(r)$, where $B_\phi^{\text{BFM}}(r) = B_0 J_0[2\Theta(r/a)]$ and $B_\theta^{\text{BFM}}(r) = B_0 J_1[2\Theta(r/a)]$ correspond to the force-free cylindrical Bessel function model. The magnetic fields $B_\phi^{\text{BFM}}(r)$, $B_\theta^{\text{BFM}}(r)$, and $\langle B \rangle = \sqrt{B_\phi^{\text{BFM}}(r)^2 + B_\theta^{\text{BFM}}(r)^2}$ for this equilibrium are illustrated in Fig. 2(a) for $\Theta = 1.35$ and in Fig. 2(b) for $\Theta = 1.8$.

Rigorously, the safety factor $q(\Psi)$ is

$$q(\Psi) \equiv \frac{1}{2\pi} \int_0^{2\pi} \left(\frac{r B_t}{R B_p} \right)_s d\theta = (r/R_0) \frac{J_0[2(r/a)\Theta]}{J_1[2(r/a)\Theta]}, \quad (16)$$

and the ratio of poloidal to toroidal magnetic fields is

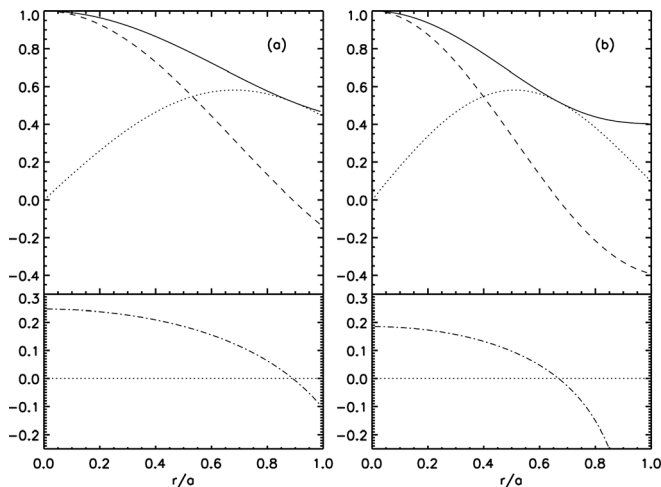


FIG. 2. Radial variation of magnetic field for (a) $\Theta = 1.35$ and (b) $\Theta = 1.8$. Both figures illustrate the total field, $\langle B \rangle$ (solid), toroidal B_T (dashed), poloidal B_P (dotted). The lower figure has the corresponding q profile.

$$\frac{B_\theta^{\text{TBFM}}(r, \theta)}{B_\phi^{\text{TBFM}}(r, \theta)} = (r/R_0) \frac{J_1[2(r/a)\Theta]}{J_0[2(r/a)\Theta]} = r/R_0 q(r), \quad (17)$$

independent of θ . The right hand side of Eq. (17), $[r/R_0 q(r)]$, can be called the the *nonzero- Θ -RFP* parameter; when $\Theta \rightarrow 0$ and $r/R_0 q(r) \rightarrow 0$, the poloidal field $B_\theta^{\text{TBFM}} \rightarrow 0$ and the toroidal field $B_\phi^{\text{TBFM}}(r) = (R_0/R) B_0$, which is the tokamak limit of the TBFM. The so-called tokamak s - α model corresponds to a large-aspect-ratio shifted circular tokamak equilibrium with the magnetic shear $s = (r/q) dq/dr$ and $\alpha = -q^2 R_0 d\beta/dr$ quantifying the Shafranov shift. More precisely when $\Theta \rightarrow 0$ [small r/R_0 and/or larger $q(r)$], the TBFM reduces to the tokamak s - α model, but with $\alpha = 0$, since the shift has been neglected in the TBFM.

When Θ increases beyond about 1.2, the toroidal field at the wall $B_\phi^{\text{TBFM}}(a, \theta)$ reverses direction. The reversal surface r_{rev}/a , where $B_\phi^{\text{TBFM}}(r_{\text{rev}}, \theta) = 0$ [the first zero of $J_0(2\Theta r/a)$] and $q(r_{\text{rev}}) = 0$, moves inward. For $r > r_{\text{rev}}$, $q(r)$ and $B_\phi^{\text{TBFM}}(r, \theta)$ are negative as illustrated in Fig. 2. The tokamak shear parameter $s(r)$ is typically negative for $r \ll r_{\text{rev}}$, small and positive for $r \gg r_{\text{rev}}$, and singular at $r = r_{\text{rev}}$ where $dq/dr < 0$ and $q = 0$, and hence $1/q \rightarrow \pm\infty$. In Sec. III, we show that no singularities occur in the TBFM formulation of the gyrokinetic equation operators since factors of $1/q$ always appear in the combination $(1/q)/[1 + (r/R_0 q)^2]^{1/2}$, which is finite at $r = r_{\text{rev}}$.

C. Breakdown of the TBFM at high Θ

A few comments are in order for high- Θ (>3) RFP regimes usually observed in discharges with external current profile control. At these values, the approximation used in Sec. A, Eq. (8), breaks down and large-aspect-ratio, higher order $O[(r/R_0)^2]$ terms must be considered. For these high- Θ discharges the numerical equilibria differ considerably from the TBFM. While large Θ is nominally far from a tokamak, as illustrated in Fig. 4, the local Miller equilibrium,¹⁷⁻¹⁹ already embedded in GYRO, can be used nonetheless (in principle) for any toroidally symmetric RFP discharge. The Miller equilibrium is a generalization of the large (infinite)-aspect-ratio, shifted circular tokamak s - α model to include the finite-aspect ratio effects of an elongated ellipse with triangularity. In essence, profiles of q , κ , δ , R_0 (safety factor, elongation, triangularity, and surface center major radius), plasma pressure (temperature and density), and the outboard-midplane toroidal field must be fitted to an experimental RFP equilibrium as a function of midplane minor radius r , where r is used as a flux surface label. This is straightforward for simulations of local linear modes and nonlinear fluctuations on either side of the reversal surface (as demonstrated in Sec. IV). In principle, global GYRO gyrokinetic simulations overlapping the reversal radius could be carried out. In practice, as we explain in Sec. III, GYRO is currently set up to read plasma and MHD equilibrium profiles keyed to the toroidal flux label χ (which is convenient for tokamaks) rather than the poloidal flux label Ψ (which is more convenient for RFPs). For RFP equilibria with toroidal field reversal, χ is not monotonic in r [note $q(r) = d\Psi(r)/d\chi(r)$]. We

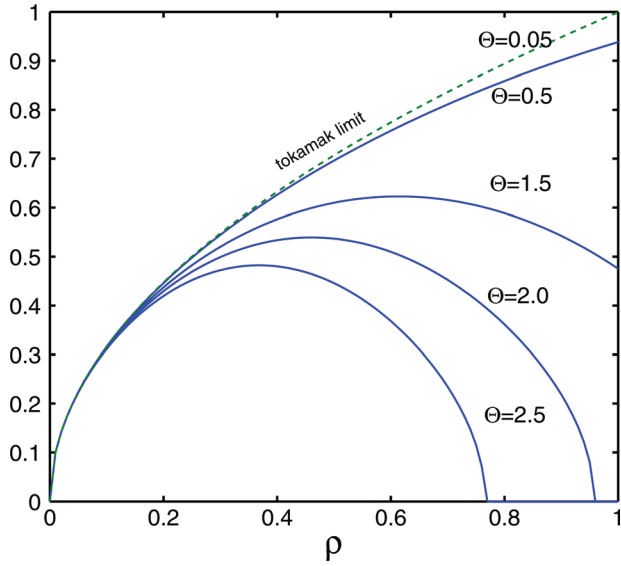


FIG. 3. (Color online) Plot of areal coordinate q vs physical coordinate \bar{r} . The dashed line indicates the limit $\Theta \rightarrow 0$, which is monotonic, and for each value of q has a unique spot in the device.

now turn to the implementation of the TBFM via the more general Miller geometry formulation of the gyrokinetic operators.

III. IMPLEMENTATION IN GYRO

For equilibrium profiles and experimental data input, GYRO uses the common tokamak areal coordinate q defined through the toroidal flux,¹⁶

$$\chi_t = \frac{1}{2\pi} \int B_\phi dA = B_0 \frac{q^2}{2}. \quad (18)$$

Here, B_0 is arbitrarily chosen as the on-axis magnetic field. For simplicity, this coordinate can be written as

$$q = a \sqrt{\frac{(r/a) J_1[2\Theta(r/a)]}{\Theta}}. \quad (19)$$

The variation of normalized q as a function of r/a is shown in Fig. 3 for several values of the pinch parameter. For sufficiently large values of the parameter Θ , the areal coordinate q may correspond to more than one flux surface. Rigorously speaking, the common tokamak profile grid q does not have a one-to-one correspondence with r/a and is not convenient for RFP experimental data profiles. Fortunately, GYRO uses r/a as the internal simulation radial grid. Furthermore for $1.91/\Theta < (r/a) < 1$, q cannot be defined in Fig. 3 because $J_1[2\Theta(r/a)] < 0$. For example, in Fig. 3, for $\Theta = 2.5$, q is not defined for $r/a > 0.76$. The other extreme ($\Theta \rightarrow 0$) is represented by a dashed line in Fig. 3 and is both monotonic and one-to-one. For RFPs, it should be straightforward to directly map experimental profiles in $\Psi(r)/\Psi(a)$ to profiles in r/a .

The choice of s and q in RFPs is also limited. In Fig. 4, the variation of q (y-axis) with s (x-axis) is illustrated for a fixed value of $\bar{r} = 0.1$ and $\varepsilon = 1/3$. The extreme top region with $q \geq 1$, which has been shaded as dark, corresponds

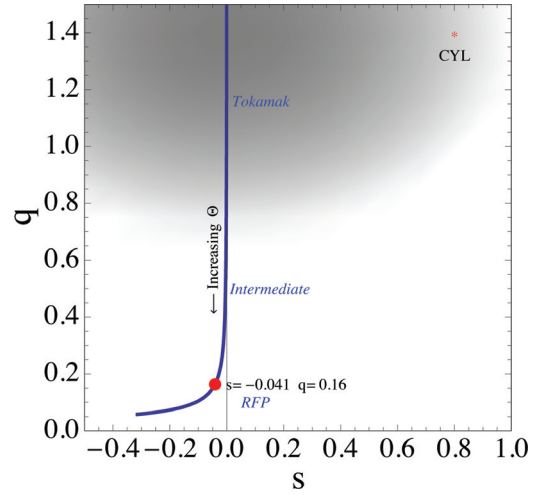


FIG. 4. (Color online) Variation of q with s . The parameter Θ has been varied for fixed $\bar{r} = 0.1$. As Θ increases, we go down the axis. The shaded region illustrates the regime of usual tokamak simulations. The red dot is the preferred point with $\Theta = 2$ and $\bar{r} = 0.1$.

to the regime of interest in usual tokamak simulations. For example, the point marked with an asterisk and labeled CYL corresponds to the usual cyclone-base case²² with $q = 1.4$ and $s = 0.8$. The $\Theta \rightarrow 0$ limit intersects this region.

Miller geometry¹⁷ has the flux surface shape defined by $R(r, \theta) = R_0(r) + r \cos\{\theta + \sin^{-1}[\delta(r)] \sin \theta\}$ and $Z(r, \theta) = r\kappa(r) \sin \theta$, where as in Eq. (5), $B_\theta = |\nabla r| \partial_r \Psi / R$ and $B_\phi = F/R$. The general formula for $|\nabla r|$ is given in Eq. (5) of Ref. 18. Since the TBFM sets the shift to $\Delta'(r) = \partial_r R_0(r)$, the elongation $\kappa(r)$ to one, and the triangularity $\delta(r)$ to zero, we have $|\nabla r|(r, \theta) = 1$, $R_0(r) = R_0(0) = R_0(a)$, and $R = R_0 + r \cos \theta$ for circular flux surfaces. Following Ref. 18, GYRO uses the midplane minor radius r (normalized to the separatrix minor radius a) as a magnetic flux surface label and primary radial grid. The primary unit of effective magnetic field strength is B_{unit} defined as

$$B_{\text{unit}}(r) = B_0 q d q / r dr. \quad (20)$$

For the TBFM model, $B_{\text{unit}}(r) = B_0 J_0[2\Theta(r/a)] = B_\phi^{\text{TFM}}(r)$, where $B_\phi^{\text{TFM}}(r, \theta) = (R_0/R) B_\phi^{\text{TFM}}(r)$ and $B_\theta^{\text{TFM}}(r, \theta) / B_\phi^{\text{TFM}}(r, \theta) = J_1[2\Theta(r/a)] / J_0[2\Theta(r/a)] = r/R_0 q(r)$.

To define the TBFM gyrokinetic operators on the ballooning mode (field-line following) field perturbations, we continue to follow Ref. 18, starting with the mode wavenumber labels and argument of the gyroaverage Bessel functions and continuing with the diamagnetic, parallel transit, and curvature drift frequency operators. For corresponding tokamak results, Ref. 16 may also be consulted.

The perpendicular wavenumber in the magnetic surface (which depends on the toroidal mode number) is

$$k_y = k_\theta[[\hat{q}]] = (n/R)(B/B_\theta) \Rightarrow k_\theta(R_0/R)[1 + (r/R_0 q)^2]^{1/2}, \quad (21)$$

where the poloidal wavenumber is $k_\theta = nq/r$. Following the $[[\]]$ notation of Ref. 18, $[[\hat{q}]](r, \theta) \equiv rB/(RqB_\theta)$. Note that $|\nabla r|[[\hat{q}]] = [[B]] = (B/B_{\text{unit}})$. The unit of ion gyroradius is $\rho_s^{\text{unit}}(r) = c_s/(eB_{\text{unit}}/m_i c)$, where $c_s(r) = (T_e/m_i)^{1/2}$. It is

useful to note that the local gyroBohm mode label at a given r becomes

$$k_{\theta}\rho_s^{\text{unit}}(r) = \frac{nq}{r} \left[\frac{c_s}{eB_{\phi}^{\text{BFM}}/m_i c} \right] = \frac{n}{R_0} \left[\frac{c_s}{eB_{\theta}^{\text{BFM}}/m_i c} \right], \quad (22)$$

so that the mode label is continuous through the reversal. Here, (n/R_0) is the toroidal wavenumber and nq/r is the poloidal wavenumber. The former is more convenient for RFPs and the latter is normally quoted for tokamaks.

The argument of the gyroaveraged Bessel function is

$$(k_{\perp}\rho_i)^2 = (2T_i/T_e)(k_{\theta}\rho_s^{\text{unit}})^2(v_{\perp}/v_{th})^2(1 + [[k_x/k_y]]^2), \quad (23)$$

where $(v_{\perp}/v_{th})^2 = \lambda[[B]]$, λ is the magnetic moment divided by the energy (pitch angle) constant of motion,

$$[[k_x/k_y]](r, \theta) \Rightarrow s(\theta - \theta_0)/[1 + (r/R_0q)^2]^{1/2}(R/R_0), \quad (24)$$

θ_0 is the ballooning mode angle label (in addition to n) and $s \equiv (r/q)dq/dr$ is the tokamak magnetic shear. The parameter $s/[1 + (r/R_0q)^2]^{1/2}$ is clearly continuous through the reversal point. The RFP-TBFM model neglects the Shafranov shift. However, to recover the tokamak s - α model in the limit $(r/R_0q) \rightarrow 0$, we could replace $s(\theta - \theta_0)$ by $s(\theta - \theta_0) - \alpha \sin \theta$.

The (flux surface constant) diamagnetic frequency operator is exactly

$$\omega_*(r) = (k_{\theta}\rho_s^{\text{unit}})(c_s/a)[a/L_n + (v^2/v_{th}^2 - 3/2)a/L_T], \quad (25)$$

where the normalized plasma density and temperature gradient scale lengths are given by $a/L_n = -ad \ln n/dr$ and $a/L_T = -ad \ln T/dr$.

The parallel motion transit frequency operator is

$$v_{\parallel}\nabla_{\parallel} \Rightarrow v_{\parallel}(1/R_0q)/[1 + (r/R_0q)^2]^{1/2}\partial_{\theta}, \quad (26)$$

which at the reversal point becomes $(v_{\parallel}/r)(|q/q)\partial_{\theta}$. (This operator is continuous given the symmetry $[v_{\parallel}, \theta] \Leftrightarrow [-v_{\parallel}, -\theta]$) Also $(v_{\parallel}/v_{th}) = \pm[(v/v_{th})^2(1 - \lambda[[B]])]^{1/2}$, and the trapped particle bounce points are $\lambda[[B]](r, \theta) = 1$.

Using the ‘‘MHD-rule’’ and setting the grad-B drift equal to the curvature drift (always true at low-beta), the ion curvature drift frequency operator is [from Eq. (19) of Ref. 18 and $|\nabla r| = 1$]

$$\omega_D(r, \theta) = \frac{T_i}{T_e}(k_{\theta}\rho_s^{\text{unit}})\frac{c_s}{a}\left(\frac{2a}{R_0}\right)\left[\left(\frac{v}{v_{th}}\right)^2\left(1 - \frac{\lambda[[B]]}{2}\right)\right] \times \{[[\cos]](r, \theta) + [[k_x/k_y]][[\sin]](r, \theta)\}. \quad (27)$$

The TBFM has factors for the geodesic curvature

$$[[\sin\theta]](r, \theta) \Rightarrow \frac{(R_0/R)\sin\theta}{[1 + (r/R_0q)^2]}, \quad (28)$$

and the normal curvature

$$[[\cos\theta]](r, \theta) \Rightarrow (R_0/R)\cos\theta + \frac{(R_0/r)(r/R_0q)^2}{[1 + (r/R_0q)^2]}. \quad (29)$$

IV. RESULTS

For simplicity, we ignore the small but finite shift in the solution given by Eq. (11), limiting ourselves to a simple equilibrium given by Eq. (10) and $\varepsilon\Delta(r/a) = 0$. Such an equilibrium has circular concentric surfaces as in the tokamak s - α model. As mentioned earlier, the essential difference between the models is the difference in the geometric factors. The geometric factors $|\nabla r|$, $[[\hat{q}]]$, $[[\cos]](r, \theta)$, B_{ϕ} , B_{θ} , $[[k_x/k_y]]$, $[[\sin]](r, \theta)$, and B for the three equilibrium models (s - α , RFP-TBFM, and the Miller geometry at $r_0/a = 0.5$) are illustrated in Fig. 5. The other parameters are $a/L_n = 0.58$, $a/L_T = 5$, and $\Theta = 1.35$, implying $q = 0.18$, $B_0 = 1$, and $s = -0.71$. The factor $[[\cos]](r, \theta)$ in Fig. 5 for the s - α model, which is shown with the symbol ‘‘+,’’ has both good curvature and bad curvature. Furthermore $B_t \sim B$, unlike the RFP.

The growth rate obtained from the TBFM greatly exceeds estimates from the usual s - α model frequently employed in tokamak studies. For a comparison, the normalized real frequency spectrum and growth rate as a function of the normalized wavenumber $k_{\theta}\rho_s$ are illustrated in Figs. 6(a) and 6(b) for the three equilibrium models. The s - α traces are indicated by the symbol +, the TBFM by the symbol \diamond , and the Miller model by a solid line. The parameters are $a/L_n = 0.58$, $a/L_T = 5$, $T_i/T_e = 0.4$, $\bar{r}_0 = 0.5$, and $\Theta = 1.35$, which corresponds to $q = 0.18$ and $s = -0.71$. The growth rate obtained from the s - α model is the least. This is because the s - α model neglects poloidal curvature and finite poloidal field, resulting in favorable curvature on the inboard side. To explain this let us look at Eq. (29) closely. In Eq. (29), the function $[[\cos]](r, \theta)$ has two terms. The first part corresponds to toroidal curvature and the second corresponds to poloidal curvature. (Note that $\varepsilon\bar{r}$ is a dimensionless quantity.) The finite poloidal magnetic field allows RFPs to have average bad curvature. The outboard side of tokamaks ($-\pi/2 < \theta < \pi/2$, $\cos(\theta) > 0$) has net bad curvature because $q > 1$ and the second term is negligible. This also results in a good curvature on the inboard side. As a result the tokamak ITG instability strongly balloons toward the outboard side. For these reasons, the s - α model assumes that $[[\cos\theta]](r, \theta) = \cos\theta$. In an RFP, the second term can exceed the first term because $q < 1$. Because this term is independent of θ , it is large everywhere, even on the inboard side. These effects are absent in simple tokamak equilibrium representation even when supplied with q values that are less than unity and negative shear.

We now examine this instability for various radial locations $r_0/a = 0.2, 0.3, 0.5, 0.65$, and 0.7 . The normalized growth rate $(\omega_i a/c_s)$ and real frequency $(\omega_r a/c_s)$ as a function of the normalized wavenumber $k_{\theta}\rho_s$ at these values of radial location are shown in Fig. 7. Other parameters are the same as before, i.e., $a/L_n = 0.58$, $a/L_T = 5$, and $T_i/T_e = 0.4$. The phase velocity ω_r/k is nearly constant and only slightly dispersive as shown in the Fig. 7(a). The phase velocity is higher at $r_0/a = 0.5$. In Fig. 7(b), the normalized growth rate $\omega_i a/c_s$ decreases dramatically at $r_0/a = 0.5$ and beyond (with gradient scale lengths kept equal). Furthermore, the range of k_{θ} with significant growth rate also decreases. At $r_0/a = 0.5$, the range is $(0 < k_{\theta}\rho_s \leq 0.6)$, which is smaller than that for $r_0/a = 0.1$. It must be noted that at these two

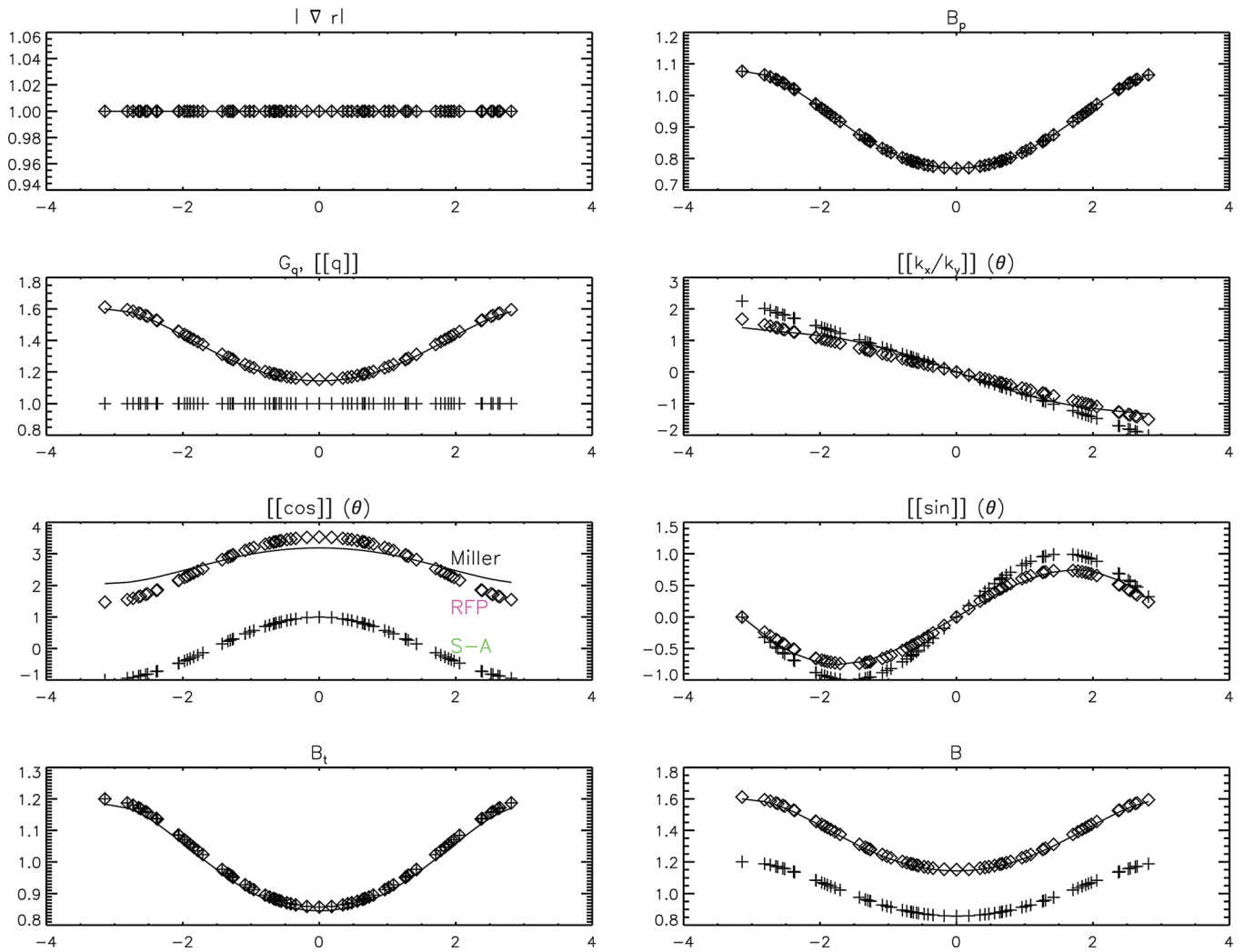


FIG. 5. (Color online) The geometric factors $|\nabla r|$, G_q , $[[q]]$, $[[\cos]](r, \theta)$, B_t , B_p , $[[k_x/k_y]]$, $[[\sin \theta]](r, \theta)$ and B for the three equilibrium models $s\text{-}\alpha(+)$, RFP toroidal Bessel function (\diamond) and Miller (solid line). The parameters are $r_0/a = 0.5$ with $\Theta = 1.35$. This corresponds to $q = 0.18$ and $s = -0.71$. Other parameters were $a/L_n = 0.58$ and $a/L_T = 5$.

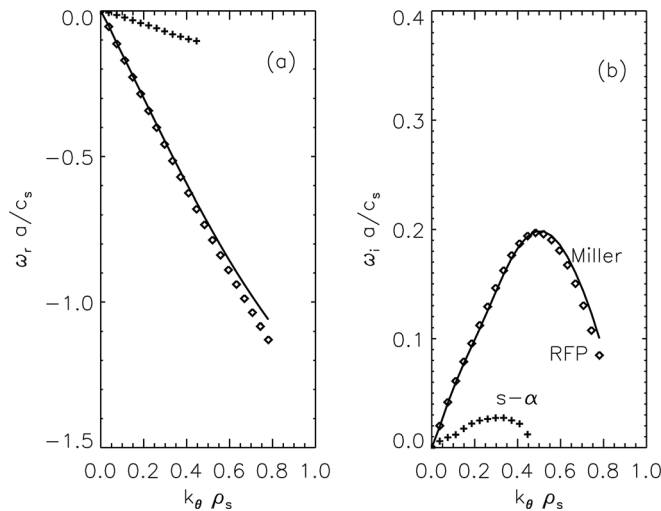


FIG. 6. (a) Normalized growth rate ($\omega_i a/c_s$) and (b) real frequency ($\omega_r a/c_s$) as a function of the normalized wavenumber $k_\theta \rho_s$ for the three equilibrium models $s\text{-}\alpha(+)$, RFP toroidal Bessel function model (\diamond) and Miller (solid line). The parameters are $r_0/a = 0.5$ with $\Theta = 1.35$. This corresponds to $q = 0.18$ and $s = -0.71$. Other parameters were $a/L_n = 0.58$ and $a/L_T = 5$.

locations, equilibrium field parameters are extremely different. While the poloidal field is small at $r_0/a = 0.2$, it is large at $r_0/a = 0.5$ and beyond. The condition for large poloidal field and associated curvature is $r_0 > r_{\text{int}}$, where $r_{\text{int}} = 2R_0q^2$. This has been estimated from $B \sim B_\phi [1 + r^2/(2R_0q^2)]$ and $r^2/(2R_0q^2) \sim r/R_0$ at $r = r_{\text{int}}$. Apart from these quantities, the magnetic shear changes dramatically while the safety factor does not. As explained in the caption of Fig. 7, in moving from $r_0/a = 0.2$ to $r_0/a = 0.7$, the safety factor q changes very less [$q(0.2) = 0.2378$ and $q(0.7) = 0.1154$] while the magnetic shear changes dramatically [$s(0.2) = -0.0775$ and $s(0.7) = -2.7552$]. Curvature also varies from surface to surface. As we move outward, the effect of geodesic curvature decreases and the effect of normal curvature increases. Beyond a certain r and Θ , there is no average good curvature at all. The poloidal contribution to curvature, $[[\cos]](r, \theta)_p = (1 + \epsilon^2 \bar{r}^2/q^2)^{-1/2} [\epsilon \bar{r}/q^2]$, is approximately 1.8 and 3.6 at the two locations, respectively. Apart from the fields, the effect of trapping, which comes from the $1/R$ variation of the field, is also different at the two locations. The Miller model and the RFP TBFM are seen to be in close agreement for $r_0/a = 0.5$ and lower. Above $r_0/a = 0.5$, the agreement

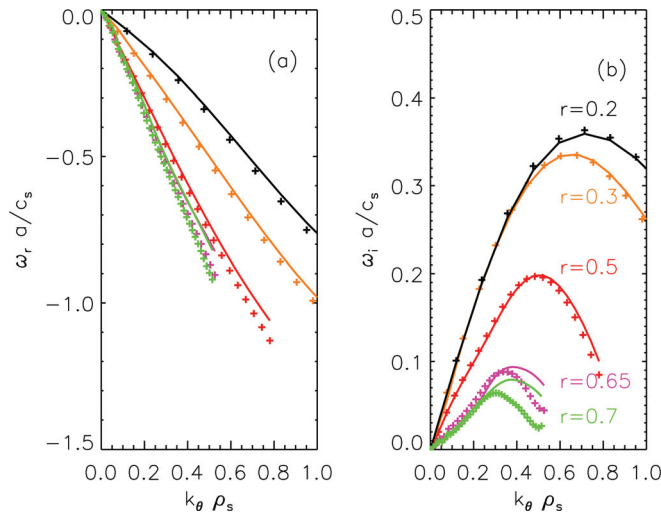


FIG. 7. (Color online) Normalized real frequency $\omega_r a/c_s$ [part (a)] and normalized growth rate $\omega_i a/c_s$ [part (b)] as a function of the normalized wave number $k_\theta \rho_s$ for $r_0/a = 0.2$, $q = 0.237$, $s = -0.0775$ (labeled $r = 0.2$); $r_0/a = 0.3$, $q = 0.226$, $s = -0.189$ (labeled $r = 0.3$); $r_0/a = 0.5$, $q = 0.1858$, $s = -0.716$ (labeled $r = 0.5$); $r_0/a = 0.65$, $q = 0.136$, $s = -1.889$ (labeled $r = 0.65$); and $r_0/a = 0.7$, $q = 0.115$, $s = -2.755$ (labeled $r = 0.7$); with Miller model (solid line) and RFP toroidal Bessel function model (+ symbols). The other parameters are $a/L_n = 0.58$, $a/L_T = 5$, and $\Theta = 1.35$.

depends on $k_\theta \rho_s$, with the TBFM yielding smaller growth rates as $k_\theta \rho_s$ increases above a critical value near $k_\theta \rho_s = 0.3$. Moreover, the critical value itself decreases as r_0/a increases from 0.65 to 0.7. The real frequency has a less significant offset between the Miller model and the TBFM.

Although GYRO does not solve the gyrokinetic equation in ballooning coordinates, the ballooning eigenvector can still be reconstructed from numerical solutions.²³ The ballooning eigenvector is illustrated in Fig. 8. The normalized real part of the eigenvector for $\Theta = 1.35$ and $\bar{r}_0 = 0.3$ is shown in Fig. 8(a) and the imaginary part in Fig. 8(b). This eigenvector is much broader than the corresponding eigen-

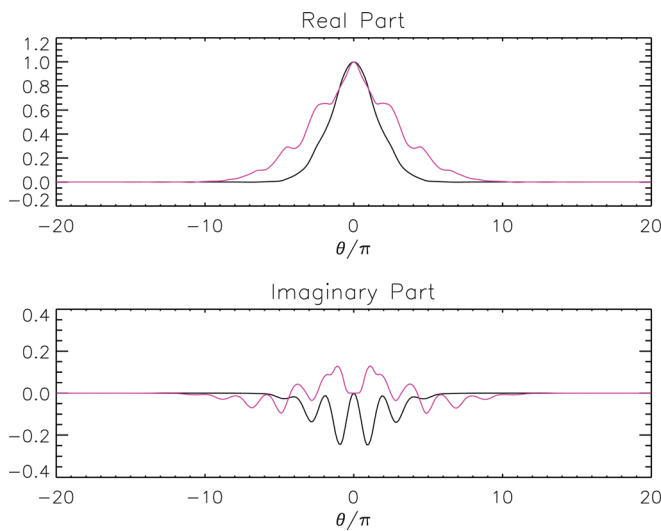


FIG. 8. (Color online) Typical normalized eigenvectors (a) real part and (b) imaginary part for $\bar{r}_0/a = 0.3$ ($q = 0.226$, $s = -0.189$) in red (gray in print), $k_\theta \rho = 0.6$, and $\bar{r}_0/a = 0.5$ ($q = 0.185$, $s = -0.716$) in black, $k_\theta \rho = 0.15$. Other parameters are $\Theta = 1.35$, $a/L_n = 0.58$, $a/L_T = 5.0$, and $T_i/T_e = 0.4$.

vector for $r_0/a = 0.5$, which is also shown for comparison. Figure 8 must also be compared with typical eigenvectors for tokamaks, which are usually very localized near $\theta_p = 0$. This is illustrated in Ref. 16, Fig. 18, where the full width at half maximum is smaller than π . On the other hand, in Fig. 8(a), it is much larger. Further details of this instability, its properties and relationship to the tokamak ITG instability will be examined in detail in a future paper.

V. CONCLUSIONS

Zero-beta solutions to the Grad-Shafranov equation assuming $(r/a)\epsilon_a/q^2 \sim 1$ and including $O(\epsilon_a)$ corrections (i.e., the poloidal variation) have been analyzed in the context of the ITG instability in RFP geometry. An average bad curvature is obtained even in the $O(\epsilon_a^0)$ variation in geometry; this differs from tokamaks away from the core. The $O(\epsilon_a)$ correction implies finite poloidal (θ) dependence of Ψ which can have significant consequences for ITG stability.

This model uses just two parameters, Θ and r/a , to represent circular shifted equilibria to $O(\epsilon_a)$ and agrees closely with numerically obtained equilibria for the MST reversed field pinch at low Θ . A simpler version of this equilibrium that neglects shift altogether is used for analytical and computational purposes to illustrate basic features of the ITG instability in an RFP. A consequence of this model is that, unlike tokamaks, the shear and safety parameters cannot be chosen arbitrarily and must satisfy the equilibrium.

Using this geometry, the gyrokinetic code GYRO has been modified to include major effects of the RFP geometry. We then compare the results with the simple $s-\alpha$ model, the more detailed RFP toroidal Bessel function model equilibria, as well as Miller equilibria. The $s-\alpha$ equilibrium predicts a much lower growth rate. Inclusion of poloidal curvature is essential to this instability. The variation of the growth rates for two different radial positions has also been examined. The growth rate is found to be higher at lower values of r_0/a where poloidal field is small. If r_0/a is increased, this mode tends to be more localized (in the ballooning direction) but with a smaller growth rate, higher real frequency and propagates much faster.

ACKNOWLEDGMENTS

This work was supported by U.S. Department of Energy Grant No. DE-FG02-85ER-53212. V.T. acknowledges the help from P. Fimognari and J. Anderson for MST equilibrium data used in Fig. 9.

APPENDIX: DERIVATION OF EQUILIBRIUM

We present the approximations, assumptions, and a brief description for the equilibrium [Eqs. (12) and (13)]. This equilibrium is accurate for low Θ and agrees well with experiment (see Fig. 9). However, at high theta, a numerical equilibria must be used.

We develop the solution of the the Grad-Shafranov equation obtained analytically from the substitution of the approximation Eq. (8) into Eq. (6). The substitution yields

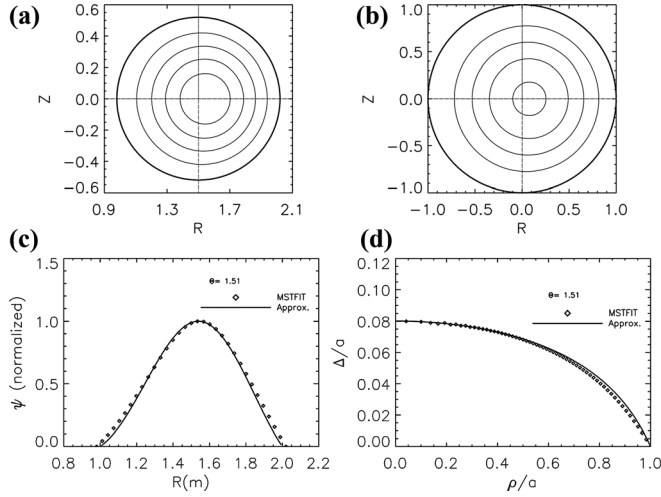


FIG. 9. Comparison of numerical and analytical equilibria. (a) Equilibrium generated from MSTFIT (Ref. 15), (b) equilibrium generated from the model, (c) comparison of normalized flux function between the model and MSTFIT, and (d) comparison of Shafranov shift for $\Theta = 1.51$.

$$\begin{aligned} & (1 + \varepsilon \hat{r} \cos \theta) \left[\frac{\partial^2}{\partial \hat{r}^2} + \frac{1}{\hat{r}} \frac{\partial}{\partial \hat{r}} + \frac{1}{\hat{r}^2} \frac{\partial^2}{\partial \theta^2} \right] \Psi \\ & - \varepsilon \left[\cos \theta \frac{\partial}{\partial \hat{r}} - \frac{\sin \theta}{\hat{r}} \frac{\partial}{\partial \theta} \right] \Psi \\ & + \mu^2 a^2 (1 + \varepsilon \hat{r} \cos \theta) (\Psi - \Psi_s) = 0. \end{aligned} \quad (\text{A1})$$

We expand the flux function and the toroidal and poloidal fields in powers of $\varepsilon \equiv a/R_0$:

$$\Psi(\hat{r}, \theta) = \Psi_0(\hat{r}) + \varepsilon \Psi_1(\hat{r}) \cos \theta, \quad (\text{A2})$$

$$B_\phi = \mu(\Psi_0(\hat{r}) - \Psi_s) + \mu \cos \theta [\hat{r}(\Psi_s - \Psi_0(\hat{r})) + \Psi_1(\hat{r})] \varepsilon, \quad (\text{A3})$$

$$B_\theta = -\frac{\Psi_0'(\hat{r})}{a} + \frac{\cos(\theta)(\hat{r}\Psi_0'(\hat{r}) - \Psi_1'(\hat{r}))}{a} \varepsilon. \quad (\text{A4})$$

Substituting Eq. (A2) into Eq. (A1), we can solve the Grad-Shafranov equation, order by order. To $O(\varepsilon^0)$, we have

$$\Psi_0''(\hat{r}) + \frac{\Psi_0'(\hat{r})}{\hat{r}} - a^2 \mu^2 (\Psi_s + \Psi_0(\hat{r})) = 0. \quad (\text{A5})$$

Assuming Ψ_0 is continuous and that $\Psi_0(\hat{r} = 0) = A$, the solution of this equation can be easily written in terms of the Bessel function $J_0(ar\mu)$,

$$\Psi_0(\hat{r}) = [1 - J_0(a\hat{r}\mu)]\Psi_s + AJ_0(a\hat{r}\mu). \quad (\text{A6})$$

Note that to this order, we have assumed a circular, unshifted equilibrium. The tokamak result in the limit of $\mu \rightarrow 0$ is obtained by expanding this in powers of μ ,

$$\Psi_0(\hat{r}) = A - \frac{1}{4} a^2 A \mu^2 \hat{r}^2 \left(1 - \frac{\Psi_s}{A} \right) \dots, \quad (\text{A7})$$

which approximately gives the $1/R$ variation as $B_T = A/R + O(\mu)^2$. In the next order, we have

$$\begin{aligned} & \Psi_1''(\hat{r}) + \frac{\Psi_1'(\hat{r})}{\hat{r}} + \left(a^2 \mu^2 - \frac{1}{\hat{r}^2} \right) \Psi_1(\hat{r}) \\ & + a\mu(A - \Psi_s) J_1(a\hat{r}\mu) = 0. \end{aligned} \quad (\text{A8})$$

The solution is

$$\Psi_1(\hat{r}) = \frac{1}{4} a \sqrt{\pi} \mu (A - \Psi_s) \mathcal{F}(z) \hat{r}^2 + J_1 c_1 + Y_1 c_2, \quad (\text{A9})$$

where

$$\mathcal{F}(z) = [\sqrt{\pi}(J_0 J_2 - J_1^2) Y_1 + J_1 \mathcal{G}(z)], \quad (\text{A10})$$

$J_i = J_i(z)$ is the Bessel function of integer order i and $z = ar\mu$ is real and positive. The function $\mathcal{G}(z)$ is the Meijer function²⁴

$$\mathcal{G}(z) = G_{3,5}^{2,2} \left(z, \frac{1}{2} \middle| 0, 1, -1, -1, -\frac{1}{2} \right), \quad (\text{A11})$$

where the notation is that of Ref. 24. It can also be written in the simplified form:

$$\mathcal{G}(z) = \frac{1}{2\pi i} \int_L \frac{\Gamma(s)\Gamma(1+s)\Gamma(1-s)\Gamma(-s)}{\Gamma(s-1/2)\Gamma(s+2)^2\Gamma(s+3/2)} z^{-2s} ds. \quad (\text{A12})$$

We define $c_1 = B_0 \delta / \mu$, and introduce a parameter δ to be determined by the boundary. We set $c_2 = 0$ because $Y_1(z)$ diverges as $\mu \rightarrow 0$ or $r \rightarrow 0$. Note that we need not make full expensive evaluations of $\mathcal{F}(z)$ and $\mathcal{G}(z)$ as all functions contained therein are functions of just one real variable z . A fit generated from a small set of equispaced values of z may be enough. Finally, from Eq. (A6) and Eq. (A9), we have

$$\Psi(\hat{r}, \theta) = \Psi_0(\hat{r}) + \varepsilon \Psi_1(\hat{r}) \cos \theta. \quad (\text{A13})$$

Now that Ψ is known accurately to $O(\varepsilon)$, this solution can be used to compute all Ψ -dependent quantities like B_ϕ , B_θ , the shift Δ , etc. The function Ψ contains several unknown constants, which are now determined. First, the $\hat{r} \rightarrow 0$ limit of Bformulas Eq. Bformulas and Eq. (A3) gives $A = (B_0 + \mu \Psi_s) / \mu$, where $B_0 = R_0 B_\phi(\hat{r} = 0)$. The parameter μ in Eq. (A6), and therefore Eq. A2), can be shown to be related to the pinch parameter Θ and F , which are defined by:

$$\Theta = \frac{\langle B_\phi \rangle^{\text{wall}}}{\langle B_\phi \rangle^{\text{vol}}} \quad \text{and} \quad F = \frac{\langle B_\phi \rangle^{\text{wall}}}{\langle B_\phi \rangle^{\text{vol}}}, \quad (\text{A14})$$

where $\langle B_\theta \rangle^{\text{wall}}$ and $\langle B_\phi \rangle^{\text{wall}}$ refer to the poloidal average of B_θ and $\langle B_\phi \rangle$ on the wall, and $\langle B_\phi \rangle^{\text{vol}}$ is the volume average of B_ϕ . Thus, it can be easily shown that

$$\Theta = \frac{a\mu}{2} + O(\varepsilon^2) \quad \text{and} \quad F = \Theta \frac{J_0(2\Theta)}{J_1(2\Theta)} + O(\varepsilon^2). \quad (\text{A15})$$

Note that all poloidal averages in Eq. (A14) come solely from terms of Eq. (A2) that are $O(\varepsilon^0)$. The boundary condition $\Psi(a, \theta) = \text{const}$ is used for $\langle B_\phi \rangle^{\text{wall}}$, but this does not mean that $B_\theta(a, \theta)$ is constant as well. Next, inverting the expression for Θ , we set $\mu = 2\Theta/a$. The $F - \Theta$ plot remains unchanged and the same as the BFM. Next, the constant Ψ_s

may be determined by the convention $\Psi = 0$ on the wall, i.e., $\Psi(1, \theta) = \Psi_0(1) = 0$, since $\Psi_1(1) = 0$ for the above value of δ . The constant is therefore given by

$$\Psi_s = -\frac{B_0}{\mu} J_0(2\Theta). \quad (\text{A16})$$

The constant δ [which is related to $c_1 = B_0\delta/\mu$ of Eq. (A9)] is determined by using the boundary condition $B_r(\hat{r} = 1, \theta) = 0$. This condition simply means that there are no fields that intersect the circular wall. From Eq. (Bformulas), this implies that $B_r(\hat{r} = 1) \propto d\Psi(\hat{r} = 1, \theta)/d\theta = 0$, or $\Psi(a, \theta) = \text{const}$. Finally, from Eq. (A13), we have $\psi_1(\hat{r} = 1) = 0$ which along with $c_2 = 0$ and Eq. (A9) gives us

$$c_1 = -\frac{a\sqrt{\pi}\mu(A - \Psi_s)\mathcal{F}(2\Theta)}{4J_1(2\Theta)}, \quad (\text{A17})$$

or

$$\delta = -\sqrt{\pi} \left(\frac{\Theta}{2} \right) \frac{\mathcal{F}(2\Theta)}{J_1(2\Theta)}, \quad (\text{A18})$$

where $A = (B_0 + \mu\Psi_s)/\mu$ has been used.

Using these formulas, Ψ may now be written

$$\Psi(\hat{r}, \theta) = \frac{B_0 a}{2} \left[\frac{(J_0(2\hat{r}\Theta) - J_0(2\Theta))}{\Theta} + \varepsilon \cos \theta \left(\frac{\sqrt{\pi}}{2} \mathcal{F}(z)\hat{r}^2 + \frac{\delta}{\Theta} J_1(z) \right) \right]. \quad (\text{A19})$$

The location of the magnetic center is obtained by expanding $\partial_{\hat{r}}\Psi = 0$, assuming that the shift is small and close to the origin (allowing us to expand the Bessel functions around zero). The magnetic center is located at

$$\Delta_0 = \varepsilon \frac{\delta}{2\Theta}, \quad (\text{A20})$$

where δ is given by Eq. (A18). The dimensionless parameter Δ_0 is proportional to the distance between the points C_m and C_g in Fig. 1. This shows that there is no shift in the limit $\varepsilon \rightarrow 0$. The values of δ given by Eq. (A18) diverge when $J_1(2\Theta) \sim 0$ or $\Theta \sim 1.9$. Therefore, if Θ is such that $J_1(2\Theta) \sim 0$ the above formulas cannot be trusted for ITG purposes. This condition equally applies to the cylindrical BFM as well. The function $\Psi(\hat{r}, \theta)$ given by Eq. (A19) as a function of R and Z is illustrated in Fig. 9 for typical MST parameters $a = 50\text{cm}$, $\Theta = 1.5$, $\varepsilon = 1/3$, and $B_0 = 1$. Note the outward shift. The peak value of Ψ at the magnetic center is given by

$$\Psi(\Delta_0) = \frac{aB_0}{2\Theta} [1 - J_0(2\Theta)]. \quad (\text{A21})$$

In a coordinate system centered at this point (as is used in GYRO), we can write, (see Fig. 1), $R = R(r) + r \cos(\theta)$ and $Z = r \sin(\theta)$. A simple transformation is given by $\hat{r} = \bar{r} + \varepsilon\Delta(\bar{r}) \cos \varphi + O(\varepsilon)^2$ and $\varepsilon \cos \theta = \varepsilon \cos \varphi + O(\varepsilon)^2$, where $\bar{r} \equiv r/a$. Substituting this into Eq. (A19) and expanding in ε , we get

$$\varepsilon\Delta(\bar{r}) = \frac{1}{4} \left[\sqrt{\pi} \frac{\mathcal{F}(2\bar{r}\Theta)}{J_1} \bar{r}^2 + \frac{2\delta}{\Theta} \right] \quad (\text{A22})$$

and

$$\Psi(\bar{r}) = \frac{aB_0}{2\Theta} [J_0(2\bar{r}\Theta) - J_0(2\Theta)]. \quad (\text{A23})$$

Note that \bar{r} and Ψ do not have one-to-one correspondence if Θ extends beyond the second zero of the function J_0 or $2\Theta > 5.52$. If that is the case, the above solutions (and therefore the BFM) cannot be trusted. Next, we can write

$$B_\phi = B_0 J_0(2\bar{r}\Theta) (1 - \varepsilon \bar{r} \cos \theta), \quad (\text{A24})$$

$$\begin{aligned} B_\theta &= -\frac{1}{R} \frac{\partial \Psi}{\partial \bar{r}} (1 - \varepsilon \cos \theta \Delta') \\ &= -\frac{d\Psi_0(\bar{r})}{d\bar{r}} (1 - \varepsilon(\bar{r} + \Delta') \cos \theta), \end{aligned} \quad (\text{A25})$$

where $\Delta' = \partial_{\bar{r}}\Delta(\bar{r})$. Finally, in this coordinate system, $B_r(a) = 0$ identically since there is no θ dependence of Ψ .

- ¹W. Horton, D. Lindberg, J. Y. Kim, J. Q. Dong, G. W. Hammett, S. D. Scott, M. C. Zarnstorff, and S. Hamaguchi, *Phys. Fluids B* **4**, 953 (1992).
- ²J. S. Sarff, S. A. Hokin, H. Ji, S. C. Prager, and C. R. Sovinec, *Phys. Rev. Lett.* **72**, 3670 (1994).
- ³S. Guo, R. Paccagnella, and F. Romanelli, *Phys. Plasmas* **1**, 2741 (1994).
- ⁴S. C. Guo, *Phys. Plasmas* **15**, 122510 (2008).
- ⁵I. Predebon, C. Angioni, and S. C. Guo, *Phys. Plasmas* **17**, 012304 (2010).
- ⁶V. Tangri, P. W. Terry, and R. E. Waltz, *Bull. Am. Phys. Soc.* **52**, 177 (2007).
- ⁷W. Horton, *Rev. Mod. Phys.* **71**, 735 (1999).
- ⁸J. B. Taylor, *Phys. Rev. Lett.* **33**, 1139 (1974).
- ⁹K. Schoenberg, R. Gribble, and J. Phillips, *Nucl. Fusion* **22**, 1433 (1982).
- ¹⁰J. Freidberg, *Ideal Magnetohydrodynamics* (Plenum, New York, 1987).
- ¹¹L. Solov'ev, *Sov. Phys. JETP* **26**, 400 (1968).
- ¹²P. J. M. Carthy, *Phys. Plasmas* **6**, 3554 (1999).
- ¹³E. K. Maschke, *Plasma Phys.* **15**, 535 (1973).
- ¹⁴J. M. Greene, *Plasma Phys. Controlled Fusion* **30**, 327 (1988).
- ¹⁵J. Anderson, C. Forest, T. Biewer, J. Sarff, and J. Wright, *Nucl. Fusion* **44**, 162 (2004).
- ¹⁶J. Candy and R. E. Waltz, *J. Comput. Phys.* **186**, 545 (2003).
- ¹⁷R. L. Miller, M. S. Chu, J. M. Greene, Y. R. Lin-Liu, and R. E. Waltz, *Phys. Plasmas* **5**, 973 (1998).
- ¹⁸R. E. Waltz and R. L. Miller, *Phys. Plasmas* **6**, 4265 (1999).
- ¹⁹R. Waltz, J. Candy, F. Hinton, C. Estrada-Mila, and J. Kinsey, *Nucl. Fusion* **45**, 741 (2005).
- ²⁰C. Estrada-Mila, J. Candy, and R. E. Waltz, *Phys. Plasmas* **13**, 074505 (2006).
- ²¹J. Anderson, Ph.D.thesis, University of Wisconsin, Madison, 2001.
- ²²A. M. Dimits, G. Bateman, M. A. Beer, B. I. Cohen, W. Dorland, G. W. Hammett, C. Kim, J. E. Kinsey, M. Kotschenreuther, A. H. Kritiz, L. L. Lao, J. Mandrekas, W. M. Nevins, S. E. Parker, A. J. Redd, D. E. Shumaker, R. Sydora, and J. Weiland, *Phys. Plasmas* **7**, 969 (2000).
- ²³J. Candy, R. E. Waltz, and M. N. Rosenbluth, *Phys. Plasmas* **11**, 1879 (2004).
- ²⁴I. S. Gradshteyn, I. M. Ryzhik, A. Jeffrey, and D. Zwillinger, *Table of Integrals, Series, and Products* (Academic Press, New York, 2007).